Polymer-derived silicon nitride aerogels as shape stabilizers for low and high-temperature thermal energy storage

Andrea Zambotti [a],*, Edoardo Caldesi [a], Massimo Pellizzari [a], Francesco Valentini [a], Alessandro Pegoretti [a], Andrea Dorigato [a], Giorgio Speranza [b], Kan Chen [c], Mauro Bortolotti [a], Gian D. Sorarù [a], Mattia Biesuz [a]

[a] Department of Industrial Engineering, University of Trento, Via Sommarive 9, 38123, Trento, Italy
[b] CMM - FBK, Via Sommarive 18, 38123, Trento, Italy
[c] Queen Mary University of London, School of Engineering and Materials Science, Mile End Rd., London, E1 4NS, UK

ABSTRACT

This work presents a new skeleton material for thermal energy storage (TES), a silicon nitride aerogel obtained through the pyrolysis of a pre-ceramic polymer. Silicon nitride offers a good combination of thermal conductivity, high-temperature resistance, and chemical inertness. The aerogel porosity can be spontaneously infiltrated with molten $NaNO_3$, which is a typical phase change material (PCM) in high-temperature TES. The $Si_3N_4/NaNO_3$ composite exhibits excellent thermal properties with a thermal energy storage efficiency of 82 %, a limited molten salt leakage, and good stability to thermal cycling. The aerogel withstands oxidation up to high temperature and is chemically inert even in contact with salts. This novel aerogel shows also a notable paraffin absorption ability (used in room temperature TES) with negligible leakage even when in contact with absorbent paper. The so-obtained composite reached $\approx$ 82.4 *vol* % of organic PCM and a thermal energy storage efficiency of $\approx$ 62 % compared to neat paraffin.

1. Introduction

According to projections on energy consumption in the European Union (EU), the EU state members must increase the renewable energy fraction up to 32.5 % by 2030 to match the target on greenhouse gas emissions reduction by 40 % compared to 1990 [1]. Besides, primary production of energy must be decreased, and the efficiency related to its use improved. One of the most relevant drawbacks of renewable energy sources (e.g. solar, photovoltaic, wind, tidal) is their time-dependent power output, which suffers from daily or seasonal fluctuations. In such a scenario, thermal energy storage (TES) is attracting a growing scientific and technological interest: it allows storage of the energy excess collected in specific periods of the day (or of the year) and its reuse later on. In other words, TES allows an efficient management of renewable energy (as in the case of solar energy collection [2]) and thermal energy, especially in household and industrial sectors [3].

While low-temperature TES is implemented in civil buildings [4–6], high-temperature TES applications ($120-600$ °C) are related to the collection, storage, and use of heat in industrial plants and furnaces or concentrated solar power systems. The thermal efficiency of different industrial plants, especially those indicated as energy-intensive (i.e. glass and concrete manufacturing, ceramic sintering, metals melting…), could be optimized capturing as much heat loss as possible through the development of smart energy systems able to efficiently release the stored energy [7,8]. Industrial furnaces currently have an average efficiency of about 60 %, so that retrofitted TES elements could have a relevant and positive effect on their performances [9].

Phase change materials are already used for these purposes because of their capability of converting large amounts of thermal energy into phase change enthalpy (or latent heat) and vice versa. Nevertheless, high melting temperature salts, typically employed for high-temperature applications, result problematic when dealing with their containment in the molten state [10]. In fact, their oxidative and corrosive nature, together with the high working temperature and high melting/crystallization volume changes, call for highly inert and thermally stable support materials able to act as shape stabilizers. While low-temperature shape-stabilized PCM composites use both inorganic and organic support materials, the abovementioned requirements are

---

fulfilled only by the formers [11,12]. Among inorganic support materials, SiO_2-based ones, such as mesoporous silica [13,14], diatomite [15–17], and vermiculite [18–20] have been extensively investigated because of their high porosity coupled with good mechanical properties and thermal stability. Also carbon-based compounds have been investigated including expanded graphite [21], carbon nanospheres [22], sponges [23], and graphene oxide [24,25]. However, the use of SiO_2-based architectures is generally limited when employing very high-temperature PCM salts because of silica enhanced corrosion and due to sintering phenomena that might significantly reduce the porosity of the supporting material. Moreover, silica-based scaffolds typically suffer from low thermal conductivity. On the other hand, C-based skeletons are prone to oxidation in contact with oxidant salts and thus they can easily degrade at high temperatures.

Polymer-derived ceramics (PDC) technologies [26] have been employed to synthesize highly porous structures [27] such as foams [28], aerogels and other mesoporous structures [29–32], cellular templates [33], and 3D-printed architectures [34–37] as well as fibrous ceramics [38], [39]. Among the different PDCs, Si_3N_4 offers a unique combination of high thermal and oxidation stability and good thermal conductivity, thus resulting as an attractive shape stabilizer for medium and high-temperature PCMs. Moreover, we have recently shown that amorphous Si_3N_4 aerogels with huge amounts of mesoporosity (>88 %) can be easily produced by using a perhydropolysilazane (PHPS) as a network-forming precursor, followed by supercritical drying and pyrolysis at 1400 °C under N_2 [40].

The present work aims to provide the first insight into the use of such ceramic aerogels as skeleton material for shape stabilization of molten salts in high- and low-temperature TES applications. For these purposes, $NaNO_3$ (melting at 306 °C) and paraffin wax (melting at 21 °C) were selected, since they can be considered a model system for high and low ([41–45]) temperature TES, respectively. In a recent work we have reported a similar use of Si_3N_4 felts constituted by fibrous nanobelts [46]. Besides the different synthesis routes with the hereby presented aerogel, the felt fibrous network was not able to prevent paraffin leaks over long periods above the melting point of the PCM, and loading the same support with sodium nitrate severely degraded the network after few thermal cycles. Moreover, the impregnation with molten $NaNO_3$ was not possible without the aid of vacuum. For this reason, we selected the silicon nitride aerogel as a valid alternative: it provides an amorphous 3D ceramic network with better mechanical properties and a macro-mesoporosity that guarantees sufficient capillary forces to prevent any PCM leakage.

2. Experimental procedures

To synthesize the silicon nitride aerogel, tutoProm® (NN 120-20(A)) was purchased from DurXtreme GmbH and used without any further purification. tutoProm® is a solution (20 wt%) of perhydropolysilazane (PHPS) in dibutyl ether (DBE, 80 wt%). The solution was loaded into a Parr digestion vessel (Model 4749-Parr Instrument Company, Moline, Il, USA) and placed in an oven pre-heated at 220 °C for 65 h to crosslink the PHPS precursor. At the end of the crosslinking process, a PHPS wet gel was recovered and was subsequently subjected to a 6-steps solvent exchange in cyclohexane (J.T. Baker, CAS: 110-82-7) before loading it into the reactor for CO_2 supercritical drying. First, the wet gel was washed 6 times with liquid CO_2 (10 °C, 50 bar) to allow for the solvent exchange, then the gel was supercritically dried at 43 °C and 100 bar before releasing the CO_2 at a rate < 1 bar h^{-1}. Finally, the preceramic silicon nitride aerogel was loaded in a graphite crucible and pyrolyzed at 1400 °C for 1 h in N_2 (5 °C min^{-1} – 300 cm^3 min^{-1} N_2) in a graphite furnace (Astro model, Thermal Technology LLC™, Santa Barbara, CA, USA). A more detailed description of the aerogel synthesis has been already reported in our previous work [40].

X-ray photoelectron spectroscopy (XPS) was used to determine the chemical environment of silicon and nitrogen elements present in the ceramic aerogel. N 1s and Si 2p spectra were collected using an Axis DLD Ultra spectrometer (Kratos— Manchester UK) on a wide 1300 to 0 eV range of binding energy (BE) with a 160 eV pass energy, and setting energy steps of 0.05 eV in high-resolution core line spectra acquired at 20 eV pass energy, obtaining a final energy resolution of 0.35 eV. Spectra were deconvoluted and analyzed with a home-made software based on R platform [47].

N_2 physisorption measurements were performed at 77 K with an ASAP 2020 (Micrometrics, Norcross, GA, US) nitrogen adsorption analyser to define the specific surface area (SSA) and pore size distribution of the aerogel in the 2−300 nm range. Respectively, Brunauer-Emmet-Teller (BET) and Barret-Joyner-Halenda (BJH) models were adopted for the evaluation of SSA and incremental pore volume as a function of pore radius.

Hg porosimetry was employed to define the total pore volume and dimensions in a wide range spanning from 100 μm down to 10 nm. For this purpose, a Porosimeter 2000 (Carlo Erba, Milano, Italy) was employed, setting a pressure range of 0.2−2000 bar at 20 °C. Skeletal density was determined using a He picnometry (AccuPyc 1330 TC, Micromeritics, Norcross, GA, USA). Bulk density was measured on cylindrical samples. Porosity was accordingly estimated comparing bulk and skeletal densities. The oxidation resistance of the aerogel was investigated using thermogravimetric analysis (TGA) using a Netzsch STA 409 thermobalance. The analysis was carried out in pure air flow (50 cm^3 min^{-1}) with a heating rate of 5 °C min^{-1} up to 1400 °C.

The ceramic aerogel samples were then impregnated in molten $NaNO_3$ (>99.0 %, J.T. Baker®, ACS grade, CAS: 7631-99-4) at 350 °C and in molten paraffin (Rubitherm® RT21HC) at 40 °C, showing an instantaneous intrusion of the molten PCMs into the aerogel pores. In the following, the so-obtained composites are labeled as AS (aerogel-salt) and AP (aerogel-paraffin), respectively. The mass uptake was evaluated using an analytical balance with sensitivity ±0.1 mg and measuring the weight of the sample before and after the impregnation.

The morphological features of ceramic aerogels before and after impregnation with the $NaNO_3$ salt were analyzed from fracture surfaces using a Carl Zeiss Gemini SUPRA 40 Scanning Electron Microscope equipped with a field emission gun after 10 nm Pt film deposition by sputtering.

Differential scanning calorimetry (DSC) analyses on AS specimens were performed with a Perkin Elmer DSC-7 instrument equipped with platinum crucibles, reaching 400 °C at 5 °C/min under argon at 1.5 bar. The samples were encapsulated in aluminium pans using aluminium as reference material. The thermal analyses were carried out: (i) on neat $NaNO_3$; (ii) on the AS composite just after impregnation; (iii) on the composite after a 24 h-dwelling at 350 °C (AS_24 h); (iv) on the AS composite after 10 melting/solidification cycles (AS_10c) and (v) on the AS composite after 50 melting/solidification cycles (AS_50c). The temperatures relative to the solid-solid transition between R $\overline{3}$ c to the R $\overline{3}$ m rhombohedral structures (T_{cm}, T_{mc}) and the melting-solidification phase change (T_m, T_s) of the $NaNO_3$ salt were measured. The associated enthalpies (ΔH_{cm}, ΔH_{mc}, ΔH_m, ΔH_s) were finally calculated by integration of the area of each peak.

Crystallographic data (XRD) were collected with an Italstructures IPD3000 instrument equipped with a Cobalt anode X-Ray source ($Co_{k\alpha}$ =1.788965 Å) operating at 40 kV, 20 mA, coupled with an incident beam multilayer monochromator, 1° divergence slit, and 5 °Soller slits. Diffraction patterns were acquired in reflection geometry employing an Inel CPS120 curved position sensitive detector, over the 10°-120° (2θ) range with a 0.03° channel resolution and 3600 s total counting time. Instrumental broadening was characterized using a Y_2O_3 powder (99.99 %, Sigma-Aldrich, CAS# 1314-36-9) annealed at 1400 °C for 24 hours. Rietveld quantitative analysis was performed with the software Maud [48].

The thermal diffusivity of $NaNO_3$ and AS samples was measured with a Netzsch LFA 457 MicroFlash® laser flash apparatus equipped with an

InSb sensor under a 100 mL min^{-1} Ar flow on cylindrical specimens.

The capability of the aerogel to hold the organic compound within its pores was evaluated by keeping the composite at 40 °C for 35 days on absorbing paper foils and monitoring its mass loss (AP_35). The paraffin compound chosen for impregnation presents a first transition at -5.7 °C ca. and another one at 21 °C. Since the former accounts for just 10 J g^{-1} of latent heat and is out of the temperature range of interest, only the latter transition, having 143 J g^{-1} of latent heat of fusion, has been considered in this study.

The thermal energy storage properties of neat paraffin, AP_35, AP_35 specimen cycled 30, 60 and 100 times, labeled AP_30c, AP_60c and AP_100c, respectively, were measured by DSC performing a first heating scan from -30 °C to 70 °C, followed by a cooling scan from 70 °C to −30 °C with a Mettler DSC30 calorimeter under an air flow (10 mL min^{-1}). The onset temperatures of melting and crystallization (T_m, T_c), and the specific melting and solidification enthalpy values (ΔH_m, ΔH_s) were obtained. The thermal energy storage efficiency (η) was finally determined as the ratio between the enthalpies measured in the composites and those of the neat PCM.

The thermal dynamic behavior of the AP specimen was observed with an infrared thermal imaging camera FLIR E60 (emissivity = 0.86) upon melting-crystallization ramps. The specimens were heated in an oven at 40 °C and then inserted in a refrigerator at a temperature of 5 °C; the surface temperature was then monitored for 30 min. In the same way, the specimens were cooled in a refrigerator at 5 °C and then inserted in an oven at a temperature of 40 °C.

3. Results and discussion

3.1. Ceramic aerogel characterization

Fig. 1 shows the XRD and XPS spectra of the ceramic aerogel. The diffraction pattern of the as-prepared material is given in Fig. 1a, showing the complete amorphousness of the silicon nitride aerogel.

XPS survey scans revealed the presence of Si, N and O as major elements allowing us to get information on the local chemical environment of these atoms in the amorphous aerogel structure. The binding energies were charge-referenced to the O 1s peak at 532.2 eV [49]. Oxygen is present in the sample due to the reactivity of the preceramic polymer toward O_2 and moisture. It is worth remembering that, even though the preceramic aerogel samples were stored in N_2, all the handling before pyrolysis was performed in the un-protected laboratory atmosphere. N 1s (Fig. 1b) and Si 2p (Fig. 1c) spectra confirm that the aerogel is effectively characterized by Si-N bonds whose local environment is typical for Si_3N_4. The main peaks in both spectra, 397.4 eV for N 1s and 101.7 eV for Si 2p are assigned to the abovementioned bond [50, 51]. The presence of oxygen gives rise to a shoulder at 103.0 eV relative to Si-O in the Si 2p spectrum [52], while it is slightly visible in the N 1s one as N-Si-O at 398.9 eV [53].

Bulk and skeletal densities were found to be equal to 0.34 ± 0.05 g cm^{-3} and 2.98 ± 0.10 g cm^{-3}, respectively, the latter of which is slightly smaller than that of crystalline Si_3N_4 (ρ = 3.17 g cm^{-3}) because of the amorphous nature of the aerogels and possibly due to the presence of a small fraction of silica. Accordingly, the total porosity was estimated to be ≈ 88.6 %. More details on pores distribution were acquired through nitrogen physisorption on the as-prepared skeleton material. The N_2 adsorption isotherm recorded at 77 K (Fig. 2a) shows the characteristic shape of meso-macroporous sorbents and can be assigned to a Type II isotherm following the IUPAC classification [54,55]. The thin hysteresis loop relative to capillary condensation can be assigned to a fraction of mesopores present in the aerogel. Thus, the material presents a hierarchical porous structure spanning from mesopores up to macropores. The evaluation of mesopores dimensions and volume through the BJH model resulted in a cumulative volume of pores of 0.3 cm^3 g^{-1}. Since the aerogel is expected to present an interconnected porosity, the adsorption isotherm was considered for such an evaluation, while the desorption
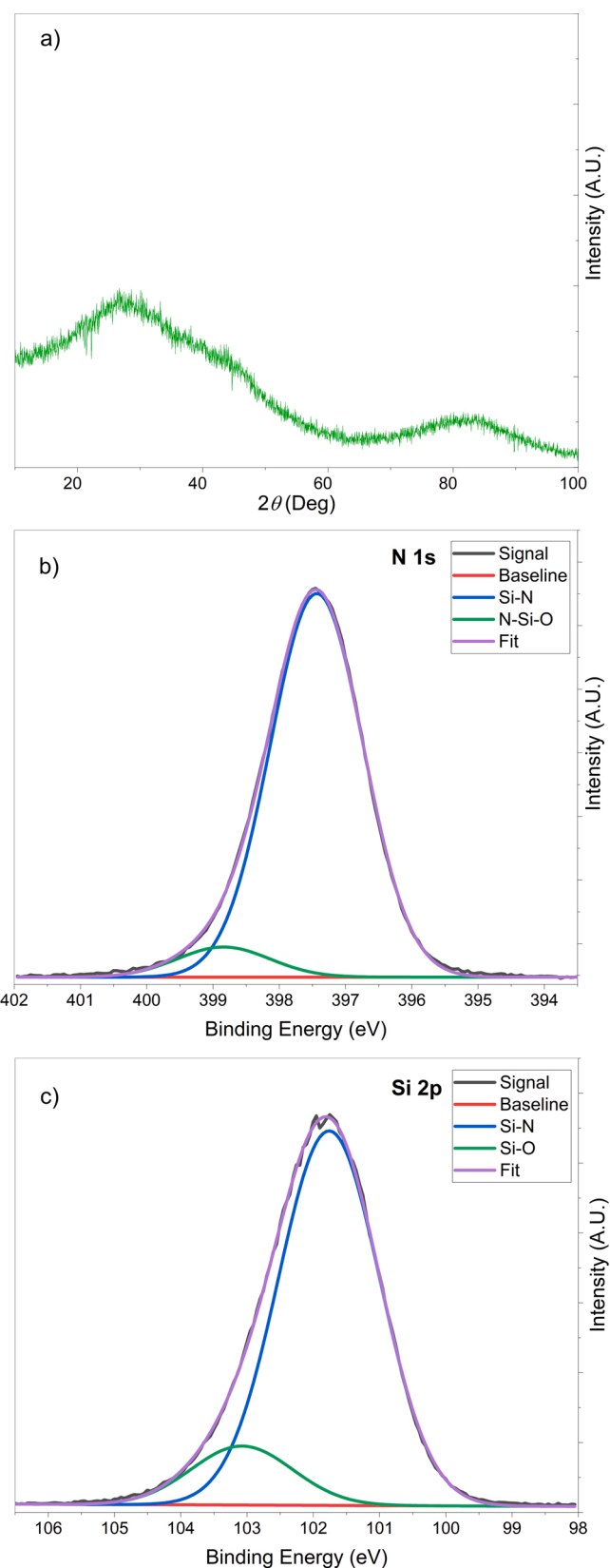

Fig. 1. Microstructural and elemental analyses of the as-prepared ceramic aerogel: a) XRD spectrum b) XPS N 1s spectrum; c) XPS Si 2p spectrum.
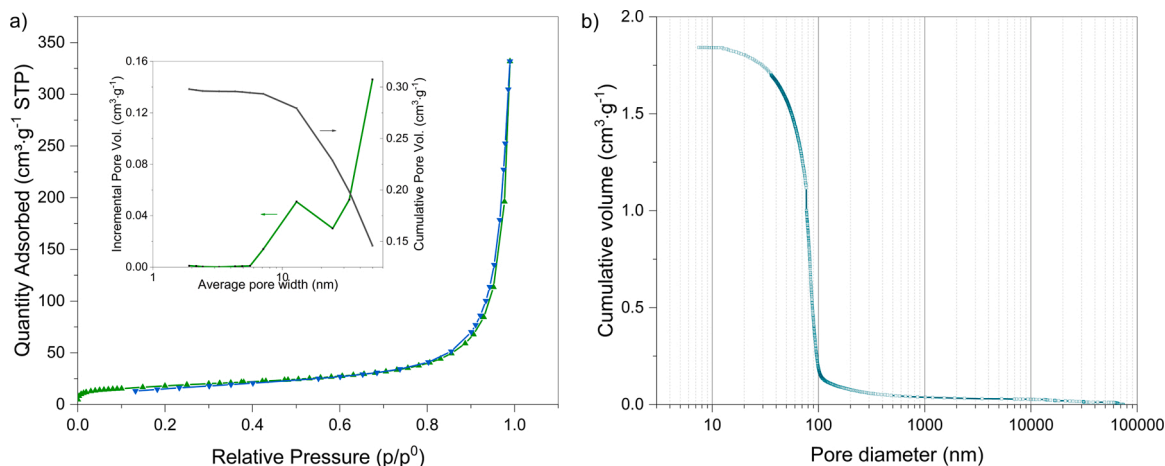
Fig. 2. a) N_2 physisorption isotherm and incremental pore volume distribution in function of the pore width; b) Hg porosimetry cumulative pore volume distribution.

one might be affected by network-percolation effects. The pore volume distribution in the function of pore width (Fig. 2a) shows that most of the mesopores have a diameter comprised between 8 nm and 30 nm. The BET specific surface area calculated at the saturation point is 63.9 m^2 g^{-1}. The SSA of the preceramic aerogel is 98.6 m^2 g^{-1} ([40]), pointing out that the high-temperature annealing at 1400 °C did not lead to a major densification of the structure. This result, together with the XRD data that revealed the amorphous nature of the material, suggests that the aerogel is very stable, in N_2 atmosphere, up to very high temperature both from the structural and microstructural point of view.

Additional data on pore distribution in the range $10-100000$ nm were acquired through Hg porosimetry (Fig. 2b). Results of the analysis confirm that the aerogel possesses a hierarchical porosity in the meso-macro range with a total cumulative pore volume (V_p) of 1.842 cm^3 g^{-1}, with 93.6 % of volume comprised in the $10-100$ nm pore radius range. The total pore volume measured from the Hg porosimeter is higher than that obtained from the N_2 physisorption analysis since the latter technique cannot sample large macropores. The total porosity P, expressed as the ratio between pore volume (V_p) and total volume (V_t) as given in Eq. 1, is 84.5 %, is in good agreement with the value of 88.6 % estimated comparing the bulk and skeletal densities.

$$P(\%) = V_p \Big/ \left(V_p + \frac{1}{\rho_s}\right) \cdot 100 = V_p \Big/ V_t \cdot 100 \qquad (1)$$

The small difference between the two values could be due to the fact that Hg cannot penetrate into the smallest pores, say <5 nm, which are also likely present in the material, albeit in a very small amount. The main results of picnometry, Hg porosimetry, and N_2 physisorption are summarized in Table 1.

The morphology of the as-prepared ceramic aerogel was observed with SEM (Fig. 3). The micrograph shows that the structure is
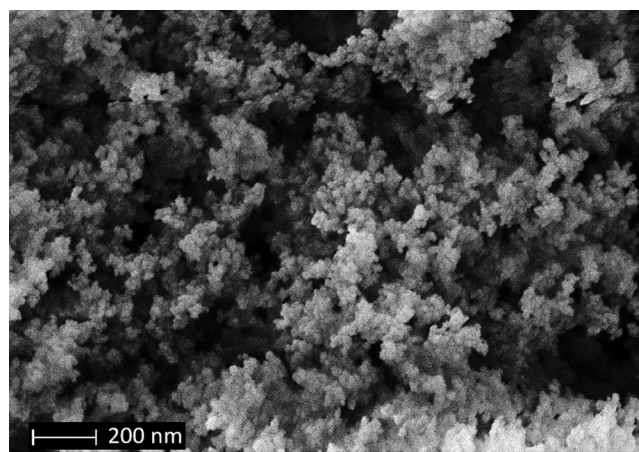
Table 1
Main properties of the ceramic aerogel as found through He picnometry, Hg porosimetry, and N_2 physisorption.

Ceramic aerogel property	Value
Bulk density, ρ_b (g cm^{-3})	0.34 ± 0.05
Skeletal density, ρ_s (g cm^{-3})	2.98 ± 0.10
Total cumulative volume, V_p (cm^3 g^{-1})[a]	1.84
Average pore radius (nm)[a]	45.0
Porosity, P (%)	$88.6^b - 84.5^a$
BET SSA (m^2 g^{-1})[c]	63.9
Average mesopore radius (nm)[c]	22.5

[a] Hg porosimetry result.
[b] He picnometry.
[c] N_2 physisorption result.

Fig. 3. FESEM images of silicon nitride aerogel.

characterized by colloidal particles with a highly interconnected porosity typical of aerogels.

3.2. Ceramic aerogel-NaNO$_3$ composites

The molten $NaNO_3$ impregnation of the ceramic aerogel was extremely rapid (completed in less than 1 min) and spontaneous. This represents a key advantage for this novel material as in most cases impregnation of the porous structures used as shape stabilizers in TES is not trivial (i.e., often requires surface factualization or vacuum impregnation). After impregnation, the mass fraction of the salt in the shape-stabilized composite reached 83.5 *wt*%. Knowing the density of the salt, 2.26 g cm^{-3} [56], its volumetric fraction was estimated ≈ 76.1 *vol*%. This means that about 12.5 *vol*% (total porosity 88.6 %) remained unfilled with the salt in the solid-state. Taking into account that the volume change of $NaNO_3$ during solidification is ≈ 9.7 *vol*% ([57]) and, considering the thermal expansion of $NaNO_3$ in the solid phase, the total volumetric variation from liquid (at the melting temperature) to solid at room temperature is about 18.9 *vol*% [58]. We can therefore deduce that the liquid salt completely infiltrated the open porosity of the aerogel and possibly some extra salt remained deposited on the aerogel surface in the form of a thin liquid film.

Fig. 4 shows a fracture surface of the $NaNO_3$-impregnated aerogel (AS specimen). The composite appears as an almost fully dense solid, where the solid salt embeds colloidal Si_3N_4 particles of the aerogel structure. The SEM micrograph substantially confirms the effective impregnation of the shape stabilizer.

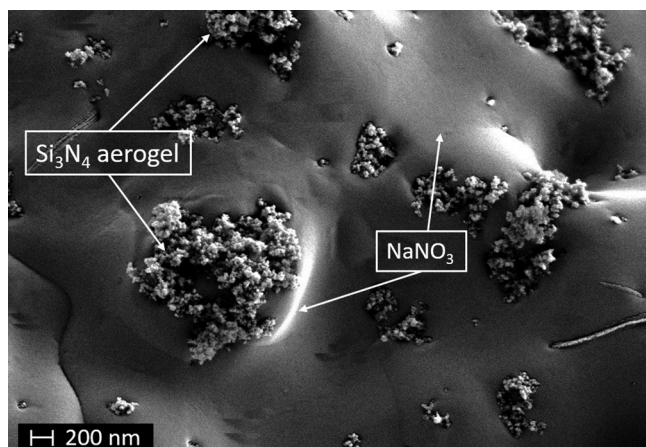**Fig. 4.** FESEM micrograph of Si_3N_4 aerogel-$NaNO_3$ composite indicating the Si_3N_4 support material and the PCM salt.

Table 2

Enthalpic data of pure $NaNO_3$ and the PCM composite (as prepared, after 10 cycles, after 50 cycles, after 24 h at 350 °C).

Samples	R3c to R3m		Melting		Efficiency on Melting
	ΔH_{cm} (J g^{-1})	T_{cm} (°C)	ΔH_m (J g^{-1})	T_m (°C)	η (%)
$NaNO_3$	43.6	273.0	179.5	305.7	–
AS	36.4	272.3	147.8	301.8	82.3
AS_10c	37.0	272.1	145.9	302.5	81.3
AS_50c	34.8	267.0	145.7	300.2	81.2
AS_24 h	36.3	271.4	145.3	303.8	80.9

DSC measurements were performed on neat $NaNO_3$, AS, AS_10c, AS_50c, and AS_24 h specimens to spot any molten salt leakage or deterioration of the thermal properties of the composite. Results of the heating steps of DSC cycles are reported in Fig. 5. As expected, the characteristic DSC curve of $NaNO_3$ presents a first endothermic peak at 273.0 °C, relative to a structural order-disorder phase transition from the R $\bar{3}$ c to the R $\bar{3}$ m rhombohedral structure [59]. The enthalpy involved in this transition is reported to be 42.3 J g^{-1} [60]. Once reached 305.7 °C, $NaNO_3$ begins the melting process. In the DSC curve, this melting phenomenon is defined by an endothermic peak characterized by a mean calculated enthalpy value of 178 J g^{-1}. All results regarding enthalpic data and transformation onset temperatures are collected in Table 2 and match the ones reported in the scientific literature [57].

For what concerns the composite performances on heating, AS shows 147.8 J g^{-1} of specific energy of fusion, while AS_24 h and AS_50c are characterized by 145.3 J g^{-1} and 145.7 J g^{-1} respectively. The absence

of a substantial difference between the as-prepared composite and the others enlightens the aerogel capability of keeping the molten salt within its pores, without any significant leakage or degradation. The net mismatch between the enthalpy of fusion of neat PCM and AS results equal to 17.6 %, which is coherent with the salt mass uptake of 83.5 *wt%* after impregnation. The difference between the $NaNO_3$ *wt%* in the composites and the thermal energy storage efficiencies measured by DSC does not exceed 1%. This result is an indication of good chemical compatibility between salt and aerogel and reveals the lack of the mismatch typically induced by the non-freezing layer at the interface between pore walls and solid PCM [61]. As a matter of fact, a highly defective interphase is reported to form in most of the PCM composites [62–64], the effect of which is to decrease the fraction of energy that can be stored. We can also spot that no degradation of the thermal energy storage properties can be detected in the AS_24 h and AS_50c samples, confirming the inert nature of the shape stabilizer and the absence of any reaction with the PCM. It is also important to point out that the phase change temperatures of $NaNO_3$ are substantially not influenced by the impregnation of the PCM in the aerogel, and the same conclusion is valid also if aged materials are considered. Data on crystallization are summarized in Table S1 of Supplementary Material.

To further prove the chemical stability of the composite, XRD spectra were collected on the AS and AS_24 h samples. The diffractograms are reported in Fig. 6, showing that ceramic aerogel and sodium salt do not
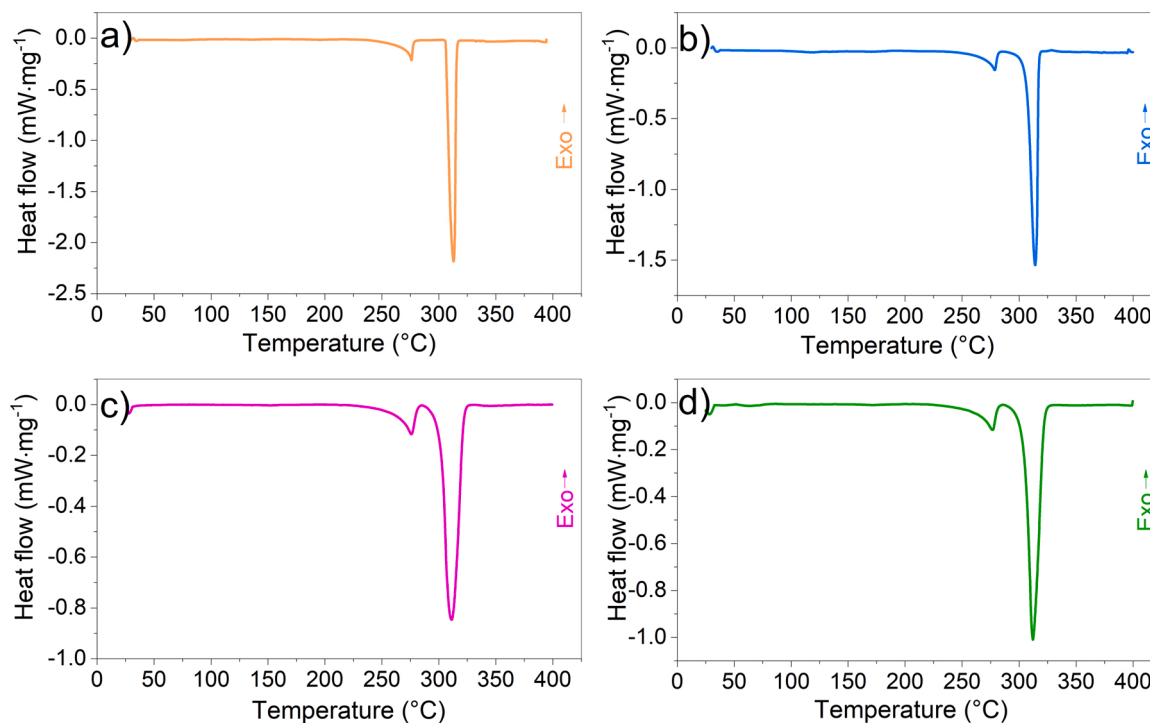

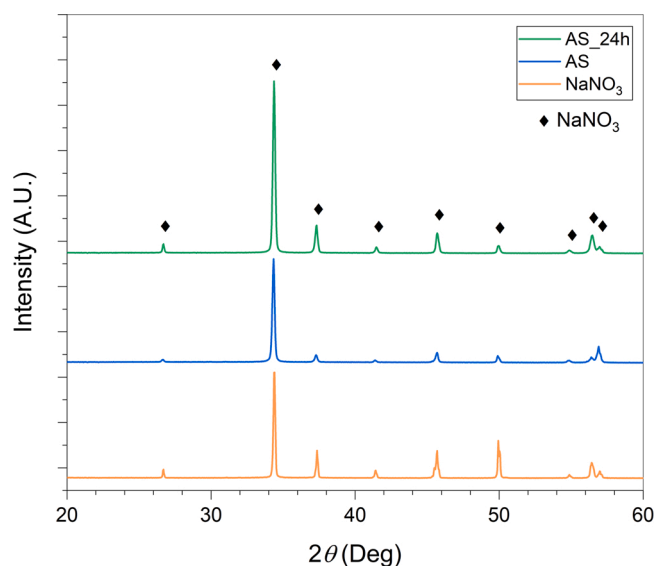**Fig. 5.** DSC heating curves of: a) Neat $NaNO_3$; b) AS; c) AS_50c; d) AS_24 h.

Fig. 6. XRD spectra of neat NaNO$_3$, AS and AS_24 h composites.

Fig. 7. Thermal diffusivity of neat NaNO$_3$ and AS composite up to 250 °C.

react at service temperature. In fact, all the measured Bragg peaks belong to the NaNO$_3$ crystal phase (ICDD No. 36-1474), as confirmed also by Rietveld modeling. The latter was performed refining background and scale parameters as well as lattice constants and average volume-weighted crystallite size [65]; refined values are reported in Table 3. As can be observed, the crystallographic and microstructural parameters of the NaNO$_3$ and AS samples are almost identical, with only a small decrease in average crystallite size and an almost negligible cell volume increase for what concerns the composite. This further confirms the substantial ability of NaNO$_3$ to perfectly recrystallize in the stable R$\overline{3}$ c form inside the composite.

The thermal diffusivity (α) of the AS composite and of the neat salt are compared in Fig. 7. As expected, thermal diffusivity is slightly affected by the presence of the ceramic support: the $\Delta\alpha$ is 0.1 mm^2 s^{-1} at 20 °C and becomes irrelevant at service temperatures. Such a behavior can be tentatively attributed to the presence of a fraction of unfilled porosity that decreases as sodium nitrate expands when temperature increases, thus reducing the thermal properties mismatch between neat salt and composite at the service temperature. At 250 °C, the measured thermal diffusivity of the AS composite is 0.13 mm^2 s^{-1}, while NaNO$_3$ reaches 0.14 mm^2 s^{-1}. The overall decrease of thermal diffusivity with temperature is given by phonon scattering phenomena that reduce the thermal transport efficiency. Therefore, using the aerogel as support material does not affect the salt thermal diffusivity, resulting to be acceptable for this kind of application. Remarkably, PDC routes allow to produce different ceramics aerogels in the Si-C-N-B system incorporating a turbostratic carbon phase, whose load depends on the preceramic resin chemistry. Thus, future research activities could focus on the optimization of the thermal conductivity of the skeletal material, in particular focusing on systems containing stabilized sp2 carbon [66].

Finally, the thermal stability of the neat aerogel and the AS composite was explored through TG-DTA measurements (Fig. 8) to define their oxidation/degradation temperatures. Fig. 8a refers to the neat Si$_3$N$_4$ aerogel when brought to high temperature under oxidative

atmosphere (air). The ceramic can withstand oxidation until 1050 °C, where is starts to gain weight due to the oxidation of Si$_3$N$_4$ into SiO$_2$. A final weight gain of 23 % is reached at 1270 °C, a temperature at which oxidation can be considered complete (as confirmed by the end of the weight gain the TGA plot). On the other hand, Fig. 8b shows the thermal degradation of AS specimen under fluxed air, which starts slightly above 500 °C, in correspondence with an exothermic peak. This peak cannot be attributed to the decomposition of NaNO$_3$ into NaNO$_2$ releasing O$_2$ (Reaction 1) that is an endothermic reaction starting at $\approx$ 600 °C [67].

$$2NO_3^- \rightleftharpoons 2NO_2^- + O_2 \qquad (1)$$

Thus, we can attribute it to the oxidation of silicon nitride through the intermediate formation of silica that is further dissolved into sodium silicate. Such a reaction occurs rapidly in the 500−700 °C temperature range because of the continuous supply of molten salt, which hinders the formation of passive layers of SiO$_2$ and Si$_2$N$_2$O, which are typical for Si$_3$N$_4$ oxidation, by dissolving them [68]. In this case, the oxidation of the skeleton material is not associated with weight gain since oxygen is supplied directly by the molten salt rather than by the atmosphere. A series of endothermic effects can further be assigned to the degradation of the molten salt into Na$_2$O, O$_2$ and NO$_2$ [69]. At 850 °C thermal degradation is completed with a total weight loss of 65 %. To further prove that the early oxidation of Si$_3$N$_4$ occurs because of the presence of sodium nitrate, TG/DTA analyses of neat the aerogel and AS under argon flux can be found in the *Supplementary material* section (Fig. S1a,b), showing the inertness of the support material and its degradation over 500 °C due to the salt, respectively. We can conclude that this novel composite can be used up to 500 °C, well above the melting point of NaNO$_3$. A comparison between the thermogravimetric analyses of neat NaNO$_3$ and a reference NaNO$_3$-αSi$_3$N$_4$ mixture, confirming the results obtained with the silicon nitride aerogel, can be found in the *Supplementary material* section (Fig. S2a,b).

3.3. Ceramic aerogel-paraffin composites

The ceramic aerogel impregnation by molten paraffin was extremely rapid and effective. The paraffin load in the composite just after impregnation was 64.5 *wt*%, equal to 82.4 *vol*%, while a 6.2 *vol*% of porosity was left empty. This could be related to a volumetric shrinkage upon freezing, or to the intrinsic difficulty for such a viscous compound to fill the smallest mesopores.

The potentiality of the new shape stabilizer to avoid molten PCM leakage thanks to its particular pore morphology was investigated by keeping the aerogel-paraffin composite at 40 °C on absorbing paper for 35 days. Results of weight loss are reported in Fig. 9, showing a very

Table 3
Average volume-weighted domain size (calculated in the isotropic approximation) and lattice constants for NaNO$_3$ and AS samples as determined from Rietveld quantitative analysis.

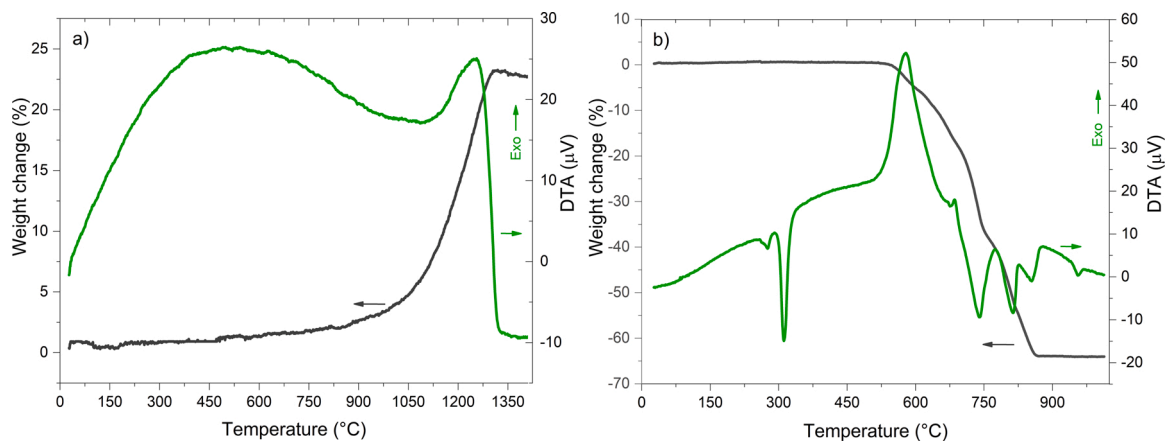|	Avg. crystallite size (nm)	a (Å)	c (Å)
NaNO$_3$	935	5.0678(6)	16.8124(6)
AS	921	5.0687(8)	16.8218(1)

Fig. 8. TG/DTA under air flux: a) pure ceramic aerogel; b) AS composite.
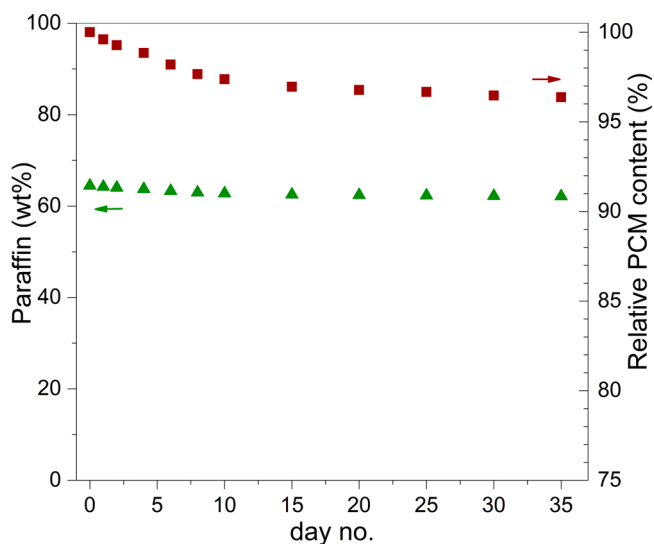

Fig. 9. Paraffin wax mass loss from AP composite along 35 days at 40 °C on absorbing paper: Paraffin weight fraction (green); Relative paraffin content with respect to day 0 (red).

Fig. 10. DSC thermograms of: neat paraffin; AP_35 composite; AP_30c; AP_60c; AP_100c.

moderate variation: after 35 days the composite still contains 62.1 *wt*% of PCM, equal to 96.4 % of the initial content. Moreover, the weight loss is mostly concentrated in the first 10 days of the leakage test. Therefore, the elevated absorption capacity of this aerogel is accompanied by a rather good PCM impregnability, properties that underline its performance compared to similar PCM composites (no comparisons with other aerogels can be made since, to the best of our knowledge, this is the first reported case). It seems that the affinity of silicon nitride to paraffin and its meso-macroporosity can be directly related to the almost complete mass uptake without the support of vacuum impregnation (which is extensively used in the case of inorganic supports) and to the absence of significant PCM leakage, which is a remarkable result with respect to other support materials. In fact, mesoporous supports have been pointed out as the best to prevent PCM leakages, while more common materials like bentonite, zeolites, and diatomites suffer from serious leaking from macropores and intergranular space [70]. This is also the case of the Si_3N_4 felts we produced: the PCM loss after 44 days at 15 °C over paraffin melting temperature reached around 15 *wt*% without showing a plateau, meaning that such structure is not optimal for the retainment of a phase change material [46].

Fig. 10 shows the DSC curves of neat paraffin and AP specimens. The calorimetric analysis revealed that the thermal performances of the composite are coherent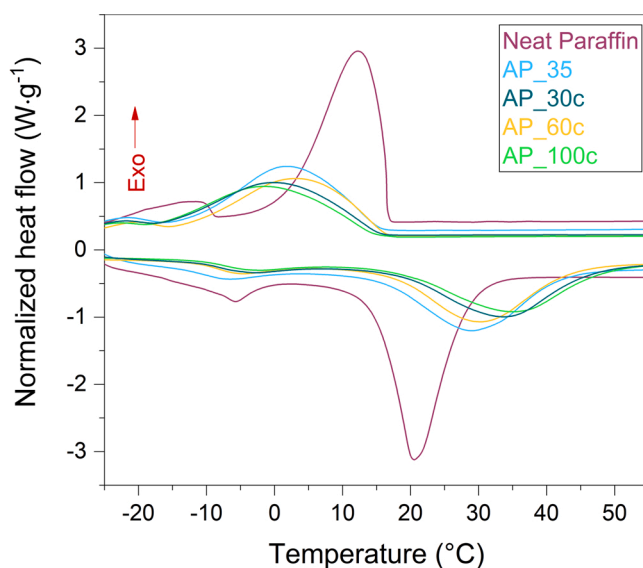 with the paraffin mass uptake defined through weight measurements, i.e. the enthalpy relative to the solid to liquid phase transition in the AP_35 specimen is 87.1 J g^{-1}, which is 62.4 % of the neat paraffin value 139.5 J g^{-1}. Considering that the mass fraction of paraffin in the AP composite is 62.1 %, there is an excellent agreement between the DSC experimental result and the theoretical melting enthalpy of paraffin within the aerogel, i.e. 86.5 J g^{-1}. The performances of the composite were monitored after 30, 60, and 100 freeze-thaw cycles. Results show no detrimental effects on the thermal efficiency of the composite, which resulted equal to 62.0 % after 100 cycles, coherently with the mass content of 62.1 %. The most important results

Table 4

DSC results of pure paraffin and aerogel-paraffin composites (AP_35, AP_30c, AP_60c, AP_100c).

Samples	PCM mass ratio%	Melting process			Solidification process		
		ΔH_m (J g^{-1})	η (%)	T_m (°C)	ΔH_s (J g^{-1})	η (%)	T_s(°C)
Paraffin	100	139.5	–	14.7	149.7	–	17.2
AP_35	62.1	87.1	62.4	16.6	91.1	60.8	16.6
AP_30c	62.1	86.4	61.9	15.5	90.2	60.2	17.8
AP_60c	62.1	86.3	61.9	15.8	90.0	60.1	17.9
AP_100c	62.1	86.5	62.0	15.7	90.3	60.3	17.9

of DSC tests on these samples are reported in Table 4.

It is also possible to observe a shift of the onset T_m value of AP_35 towards higher temperatures with respect to neat paraffin (16.6 °C instead of 14.4 °C): it can be attributed to the lower thermal conductivity of the aerogel. For the same reason, the T_s value is slightly lower than that shown by the neat paraffin sample. These differences can be better appreciated when observing the peak temperatures recorded by the DCS analyses.

The absence of anomalous DSC peaks and the coherency in mass fraction and melting enthalpy of paraffin in the AP composite are indications of a peculiar chemical affinity of this aerogel with the selected polymer and an optimal pore size distribution for its crystallization. In the present case, the non-freezing layer that tends to build up at the polymer/support interface reducing the heat storage capacity of the composite is reduced to the minimum.

Compared to other appealing supports for organic PCMs, the produced Si_3N_4 aerogel presents specific advantages in terms of chemical affinity. Polymeric aerogels and metal-organic frameworks suffer from van der Waals interactions with organic PCMs. These interactions are fundamentally detrimental for the composite thermal performances because chemical bonds reduce the PCM mobility and its capability to crystallize, thus reducing the amount of storable heat [71–73].

XRD spectra collected on the Paraffin and AP_35 samples are reported in Fig. 11. The diffractogram of the neat paraffin is typical of a semi-crystalline material, with sharp Bragg reflections superimposed over a diffuse signal, characteristic of the amorphous/nanocrystalline fraction.

Unfortunately, no crystallographic model is available for the paraffin structure in the literature, making the quantitative analysis unfeasible. However, it is still possible to recognize the remarkable similarity of the two diffraction patterns, with two Bragg reflections corresponding to about 4.65 Å and 4.0 Å interplanar spacings, indicating that the PCM can recrystallize inside the ceramic aerogel with the same structure of the neat compound. Besides, a semi-quantitative evaluation of the average crystallite size of the PCM was performed by applying the Scherrer's equation in the hypothesis of perfectly spherical crystallites ([74]), giving values of 263 nm and 224 nm for the neat paraffin and AP_35 samples, respectively. This can be an indication of a slight decrease of average crystallite size and not necessarily the crystalline fraction, which remains likely comparable to the neat PCM, as indicated by the
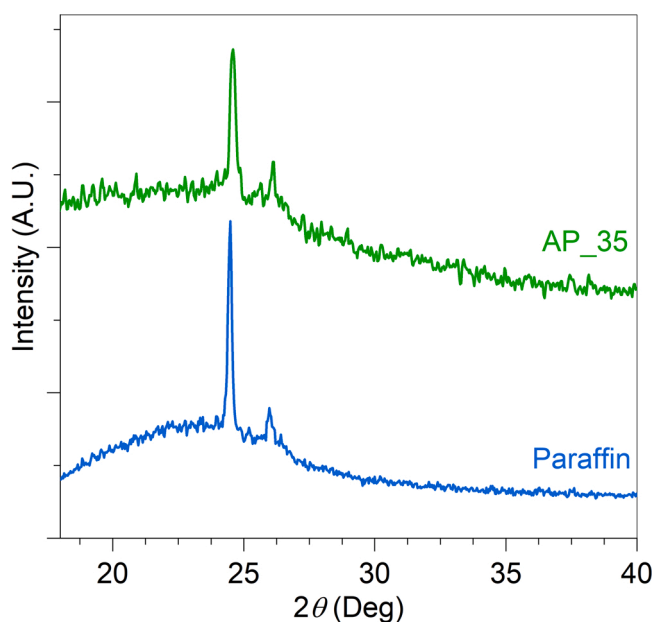

Fig. 11. Comparison of powder diffraction data acquired on neat paraffin and AP_35 samples.

thermal characterization. Finally, the affinity of the XRD spectra given in Fig. 11 confirms the absence of any induced structural disorder due to the paraffin confinement in the aerogel pores [75].

The thermal response of Si_3N_4-paraffin specimen under thermal cycles between 0 °C and 45 °C was also monitored with a thermocamera, as depicted in Fig. 12, measuring a delaying effect on temperature variation as it approaches the solid-liquid phase transition of paraffin. Both during heating and cooling the temperature stabilizes with a plateau-like trend around the melting point of the PCM. In particular, a delay of around 10 min can be defined for the AP composite under the abovementioned transitions. Such a property could be exploited for thermal regulation in buildings.

It is possible to observe that the extension of the plateau during cooling is slightly lower with respect to the one characterizing heating. The reason for this behavior can be the difference in the thermal conductivity of paraffin between the liquid and the solid-state: the higher thermal conductivity at the solid solid-state results in a more rapid crystallization process during cooling due to the faster heat diffusion through the solid [76]. On the other hand, during heating, the formation of liquid paraffin slows down the melting process.

3.4. Comparisons with the literature

Many support materials have been developed during the last few years for the containment of molten PCMs. Even if it is not simple to make a direct comparison on the thermal performances of similar composites due to the differences in the synthesis route and the PCM characteristics, in Table 5 we report a short comparison with similar works dealing with $NaNO_3$ and paraffin. Remarkably, the capacity of the aerogel to retain all the absorbed PCM is directly linkable to an efficiency similar to other as-impregnated composites but after dozens of thermal cycles.

4. Conclusions

In this paper, we reported the first application of a polymer-derived amorphous Si_3N_4 aerogel as a shape stabilizer for PCMs with intriguing properties for thermal energy storage over a wide range of temperatures. This mesoporous support material presents a porosity greater than 85 % and a BET specific surface area of 63.9 m^2 cm^{-1}. It shows no detrimental effects of the presence of a non-freezing layer at the support-PCM interface. The PCM uptake results of 76 *vol*% and 82.4 *vol*% for $NaNO_3$ and paraffin, respectively, reaching the totality of the available porosity during the impregnation process. Furthermore, no significant PCM loss was determined over thermal cycling and leakage test. This novel a-Si_3N_4 aerogel results stable toward oxidation over 1000 °C, acquiring the great technological potential to serve as a shape stabilizer for high-temperature PCMs.

The overall results prove for the first time that polymer-derived ceramics aerogels could be employed in PCM-based thermal energy storage application, thus offering a new, flexible and unexplored synthesis route toward porous and refractory shape stabilizers.

Summary of Novel Conclusion

i) The silicon nitride aerogel can be easily synthesized and impregnated with molten phase change material (PCM) without the need of vacuum. The thermal storage efficiencies of shape-stabilized sodium nitrate and paraffin are 82 % and 62 %, respectively.

ii) PCM losses are negligible even at temperatures well above their melting temperatures, keeping the thermal efficiency to a constant value even after several thermal cycles

iii) The optimal pore size distribution of the aerogel network avoids confinement effects over the crystallization of phase change
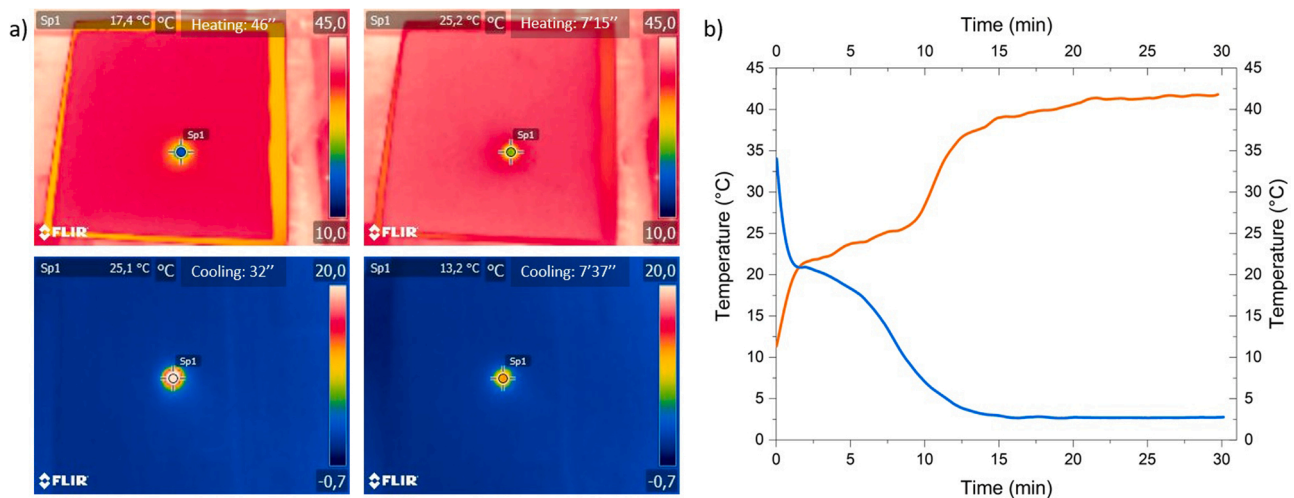
Fig. 12. Thermal response of the AP specimen subjected to heating and cooling: a) Thermal imaging on heating and cooling; b) Temperature evolution: heating (orange), cooling (blue).

Table 5

Comparison of thermal performances of similar composites. EVM = Expanded Vermiculite; EP = Expanded Perlite; CNT = Carbon Nanotubes.

Sample	Loading method	PCM wt %	ΔH_m (J g⁻¹)	T_m (°C)	Ref.
EVM/NaNO₃	Impregnation-separation	87.0	144.0	311.9	[77]
Diatomite/NaNO₃	Sintering	70.0	115.8	307.8	[78]
SiO₂/NaNO₃	Sol-gel encapsulation	81.9	144.7	310.1	[79]
Si₃N₄/NaNO₃ [a]	Ambient Impregnation	83.5	145.7	300.2	This work
EP/paraffin	Ambient Impregnation	50.0	63.5	25.3	[80]
EP-CNT/paraffin	Vacuum impregnation	60.0	157.3	36.1	[81]
Diatomite/paraffin	Pelletization	67.0	63.9	22.3	[82]
Kaolinites/paraffin	Vacuum impregnation	50.9	94.8	50.6	[83]
Si₃N₄/Paraffin	Ambient impregnation	77.4	107.7	28.2	[46]
Si₃N₄/Paraffin [b]	Ambient Impregnation	62.0	86.5	15.7	This work

[a] Data relative to AS_50c.
[b] Data relative to AP_100c.

materials, leading to just 1% mismatch between effective and theoretical thermal efficiencies.

iv) The aerogels can withstand oxidation above 1000°C in air, indicating that this material could be employed in future thermal energy storage applications even at ultra-high temperature.

Funding

This work was supported by the Italian Ministry of University and Research (MIUR) within the programs PRIN2017 - 2017FCFYHK "DIRECTBIOPOWER", PRIN2017 - 2017PMR932 "Nanostructured Porous Ceramics for Environmental and Energy Applications".

Declaration of Competing Interest

The authors report no declarations of interest.

Appendix A. Supplementary data

Supplementary material related to this article can be found, in the online version, at doi:https://doi.org/10.1016/j.jeurceramsoc.2021.04.056.

References

[1] H. Förster, et al., Trends and projections in Europe 2019: tracking progress towards Europes climate and energy targets, Publ. Office Eur. Union 15 (2019), https://doi.org/10.2800/51114.
[2] B. Stutz, et al., Storage of thermal solar energy, C. R. Phys. 18 (September (7–8)) (2017) 401–414, https://doi.org/10.1016/j.crhy.2017.09.008.
[3] X. Huang, et al., Shape-stabilized phase change materials based on porous supports for thermal energy storage applications, Chem. Eng. J. 356 (January) (2019) 641–661, https://doi.org/10.1016/j.cej.2018.09.013.
[4] J. Pereira da Cunha, P. Eames, Thermal energy storage for low and medium temperature applications using phase change materials – a review, Energy 177 (September) (2016) 227–238, https://doi.org/10.1016/j.apenergy.2016.05.097.
[5] A. de Gracia, L.F. Cabeza, Phase change materials and thermal energy storage for buildings, Energy Build. 103 (September) (2015) 414–419, https://doi.org/10.1016/j.enbuild.2015.06.007.
[6] F. Valentini, F. Morandini, M. Bergamo, A. Dorigato, Development of eco-sustainable plasters with thermal energy storage capability, J. Appl. Phys. 128 (August (7)) (2020), https://doi.org/10.1063/5.0012139, p. 075103.
[7] H. Lund, P.A. Østergaard, D. Connolly, B.V. Mathiesen, Smart energy and smart energy systems, Energy 137 (October) (2017) 556–565, https://doi.org/10.1016/j.energy.2017.05.123.
[8] A. Gil, et al., State of the art on high temperature thermal energy storage for power generation. Part 1—concepts, materials and modellization, Renew. Sustain. Energy Rev. 14 (January (1)) (2010) 31–55, https://doi.org/10.1016/j.rser.2009.07.035.
[9] P. Royo, L. Acevedo, V.J. Ferreira, T. García-Armingol, A.M. López-Sabirón, G. Ferreira, High-temperature PCM-based thermal energy storage for industrial furnaces installed in energy-intensive industries, Energy 173 (April) (2019) 1030–1040, https://doi.org/10.1016/j.energy.2019.02.118.
[10] Á.G. Fernández, L.F. Cabeza, Molten salt corrosion mechanisms of nitrate based thermal energy storage materials for concentrated solar power plants: a review, Sol. Energy Mater. Sol. Cells 194 (June) (2019) 160–165, https://doi.org/10.1016/j.solmat.2019.02.012.

[11] K. Pielichowska, K. Pielichowski, Phase change materials for thermal energy storage, Prog. Mater. Sci. 65 (August) (2014) 67–123, https://doi.org/10.1016/j.pmatsci.2014.03.005.

[12] F. Jiang, et al., Skeleton materials for shape-stabilization of high temperature salts based phase change materials: a critical review, Renew. Sustain. Energy Rev. 119 (March) (2020), https://doi.org/10.1016/j.rser.2019.109539, p. 109539.

[13] T. Nomura, C. Zhu, N. Sheng, K. Tabuchi, A. Sagara, T. Akiyama, Shape-stabilized phase change composite by impregnation of octadecane into mesoporous SiO, Sol. Energy Mater. Sol. Cells 143 (December) (2015) 424–429, https://doi.org/10.1016/j.solmat.2015.07.028.

[14] T. Qian, J. Li, X. Min, Y. Deng, W. Guan, L. Ning, Radial-like mesoporous silica sphere: a promising new candidate of supporting material for storage of low-, middle-, and high-temperature heat, Energy 112 (October) (2016) 1074–1083, https://doi.org/10.1016/j.energy.2016.07.023.

[15] Y. Deng, J. Li, T. Qian, W. Guan, X. Wang, Preparation and characterization of KNO3/diatomite shape-stabilized composite phase change material for high temperature thermal energy storage, J. Mater. Sci. Technol. 33 (2 Febuary) (2017) 198–203, https://doi.org/10.1016/j.jmst.2016.02.011.

[16] S. Karaman, A. Karaipekli, A. Sarı, A. Biçer, Polyethylene glycol (PEG)/diatomite composite as a novel form-stable phase change material for thermal energy storage, Sol. Energy Mater. Sol. Cells 95 (July (7)) (2011) 1647–1653, https://doi.org/10.1016/j.solmat.2011.01.022.

[17] Z. Sun, Y. Zhang, S. Zheng, Y. Park, R.L. Frost, Preparation and thermal energy storage properties of paraffin/calcined diatomite composites as form-stable phase change materials, Thermochim. Acta 558 (April) (2013) 16–21, https://doi.org/10.1016/j.tca.2013.02.005.

[18] B. Xu, H. Ma, Z. Lu, Z. Li, Paraffin/expanded vermiculite composite phase change material as aggregate for developing lightweight thermal energy storage cement-based composites, Appl. Energy 160 (December) (2015) 358–367, https://doi.org/10.1016/j.apenergy.2015.09.069.

[19] Y. Deng, J. Li, T. Qian, W. Guan, Y. Li, X. Yin, Thermal conductivity enhancement of polyethylene glycol/expanded vermiculite shape-stabilized composite phase change materials with silver nanowire for thermal energy storage, Chem. Eng. J. 295 (July) (2016) 427–435, https://doi.org/10.1016/j.cej.2016.03.068.

[20] C. Li, H. Yang, Expanded vermiculite/paraffin composite as a solar thermal energy storage material, J. Am. Ceram. Soc. 96 (September (9)) (2013) 2793–2798, https://doi.org/10.1111/jace.12504.

[21] Y. Ren, C. Xu, M. Yuan, F. Ye, X. Ju, X. Du, Ca(NO3)2-NaNO3/expanded graphite composite as a novel shape-stable phase change material for mid- to high-temperature thermal energy storage, Energy Convers. Manage. 163 (May) (2018) 50–58, https://doi.org/10.1016/j.enconman.2018.02.057.

[22] M. Mehrali, S. Tahan Latibari, M. Mehrali, T.M.I. Mahlia, H.S. Cornelis Metselaar, Effect of carbon nanospheres on shape stabilization and thermal behavior of phase change materials for thermal energy storage, Energy Convers. Manage. 88 (December) (2014) 206–213, https://doi.org/10.1016/j.enconman.2014.08.014.

[23] T. Chen, et al., Fatty amines/graphene sponge form-stable phase change material composites with exceptionally high loading rates and energy density for thermal energy storage, Chem. Eng. J. 382 (Febuary) (2020) 122831, https://doi.org/10.1016/j.cej.2019.122831.

[24] J. Yang, et al., Hybrid graphene aerogels/phase change material composites: thermal conductivity, shape-stabilization and light-to-thermal energy storage, Carbon 100 (April) (2016) 693–702, https://doi.org/10.1016/j.carbon.2016.01.063.

[25] Y. Cao, D. Fan, S. Lin, L. Mu, F.T.T. Ng, Q. Pan, Phase change materials based on comb-like polynorbornenes and octadecylamine-functionalized graphene oxide nanosheets for thermal energy storage, Chem. Eng. J. 389 (June) (2020), https://doi.org/10.1016/j.cej.2020.124318, p. 124318.

[26] P. Colombo, G. Mera, R. Riedel, G.D. Sorarù, Polymer-derived ceramics: 40 years of research and innovation in advanced ceramics: polymer-derived ceramics, J. Am. Ceram. Soc. (June) (2010), https://doi.org/10.1111/j.1551-2916.2010.03876.x p. no-no.

[27] C. Vakifahmetoglu, D. Zeydanli, P. Colombo, Porous polymer derived ceramics, Mater. Sci. Eng. R Rep. 106 (August) (2016) 1–30, https://doi.org/10.1016/j.mser.2016.05.001.

[28] B. Santhosh, C. Vakifahmetoglu, E. Ionescu, A. Reitz, B. Albert, G.D. Sorarù, Processing and thermal characterization of polymer derived SiCN(O) and SiOC reticulated foams, Ceram. Int. 46 (April (5)) (2020) 5594–5601, https://doi.org/10.1016/j.ceramint.2019.11.003.

[29] G.D. Sorarù, et al., Novel polysiloxane and polycarbosilane aerogels via hydrosilylation of preceramic polymers, J. Mater. Chem. 22 (16) (2012), https://doi.org/10.1039/c2jm00020b, p. 7676.

[30] C. Vakifahmetoglu, D. Zeydanli, M.D. de, M. Innocentini, Fdos S. Ribeiro, P.R. O. Lasso, G.D. Soraru, Gradient-Hierarchic-Aligned Porosity SiOC Ceramics, Sci. Rep. 7 (Febuary (1)) (2017), https://doi.org/10.1038/srep41049, p. 41049.

[31] P. Dibandjo, et al., Synthesis of boron nitride with ordered mesostructure, Adv. Mater. 17 (March (5)) (2005) 571–574, https://doi.org/10.1002/adma.200401501.

[32] S. Moldovan, O. Ersen, C. Sanchez, R. Campostrini, G.D. Sorarù, Shedding light onto the nano- and micro-structures of B-containing SiOC glasses using high resolution TEM 3D imaging, J. Eur. Ceram. Soc. 39 (August (10)) (2019) 3042–3050, https://doi.org/10.1016/j.jeurceramsoc.2019.03.044.

[33] P. Jana, O. Santoliquido, A. Ortona, P. Colombo, G.D. Sorarù, Polymer-derived SiCN cellular structures from replica of 3D printed lattices, J. Am. Ceram. Soc. 101 (July (7)) (2018) 2732–2738, https://doi.org/10.1111/jace.15533.

[34] A. Zocca, C.M. Gomes, A. Staude, E. Bernardo, J. Günster, P. Colombo, SiOC ceramics with ordered porosity by 3D-printing of a preceramic polymer, J. Mater.

[35] L. Brigo, J.E.M. Schmidt, A. Gandin, N. Michieli, P. Colombo, G. Brusatin, 3D Nanofabrication of SiOC Ceramic Structures, Adv. Sci. 5 (December (12)) (2018), https://doi.org/10.1002/advs.201800937, p. 1800937.

[36] Z.C. Eckel, C. Zhou, J.H. Martin, A.J. Jacobsen, W.B. Carter, T.A. Schaedler, Additive manufacturing of polymer-derived ceramics, Science 351 (January (6268)) (2016) 58–62, https://doi.org/10.1126/science.aad2688.

[37] A. Kulkarni, G.D. Sorarù, J.M. Pearce, Polymer-derived SiOC replica of material extrusion-based 3-D printed plastics, Addit. Manuf. 32 (March) (2020), https://doi.org/10.1016/j.addma.2019.100988, p. 100988.

[38] S. Yajima, Y. Hasegawa, J. Hayashi, and M. Iimura, Synthesis of continuous silicon carbide fibre with high tensile strength and high Youngs modulus, p. 8.

[39] M. Biesuz, et al., Polymer-derived Si3N4 nanofelts for flexible, high temperature, lightweight and easy-manufacturable super-thermal insulators, Appl. Mater. Today 20 (September) (2020), https://doi.org/10.1016/j.apmt.2020.100648, p. 100648.

[40] A. Zambotti, et al., Synthesis and thermal evolution of polysilazane-derived SiCN (O) aerogels with variable C content stable at 1600°C, Ceram. Int. (November) (2020), https://doi.org/10.1016/j.ceramint.2020.11.157. S0272884220334921.

[41] Y. Zhong, et al., Heat transfer enhancement of paraffin wax using compressed expanded natural graphite for thermal energy storage, Carbon 48 (January (1)) (2010) 300–304, https://doi.org/10.1016/j.carbon.2009.09.033.

[42] G. Fredi, A. Dorigato, L. Fambri, A. Pegoretti, Multifunctional epoxy/carbon fiber laminates for thermal energy storage and release, Compos. Sci. Technol. 158 (April) (2018) 101–111, https://doi.org/10.1016/j.compscitech.2018.02.005.

[43] D. Rigotti, A. Dorigato, A. Pegoretti, 3D printable thermoplastic polyurethane blends with thermal energy storage/release capabilities, Mater. Today Commun. 15 (June) (2018) 228–235, https://doi.org/10.1016/j.mtcomm.2018.03.009.

[44] A. Dorigato, D. Rigotti, A. Pegoretti, Thermoplastic polyurethane blends with thermal energy storage/release capability, Front. Mater. 5 (September) (2018) 58, https://doi.org/10.3389/fmats.2018.00058.

[45] G. Fredi, A. Dorigato, L. Fambri, A. Pegoretti, Wax confinement with carbon nanotubes for phase changing epoxy blends, Polymers 9 (August (12)) (2017), https://doi.org/10.3390/polym9090405, p. 405.

[46] F. Valentini, A. Dorigato, A. Pegoretti, M. Tomasi, G.D. Sorarù, M. Biesuz, Si3N4 nanofelts/paraffin composites as novel thermal energy storage architecture, J. Mater. Sci. 56 (January (2)) (2021) 1537–1550, https://doi.org/10.1007/s10853-020-05247-5.

[47] G. Speranza, R. Canteri, RxpsG a new open project for Photoelectron and Electron Spectroscopy data processing, SoftwareX 10 (July) (2019) 100282, https://doi.org/10.1016/j.softx.2019.100282.

[48] M. Bortolotti, L. Lutterotti, G. Pepponi, Combining XRD and XRF analysis in one Rietveld-like fitting, Powder Diffr. 32 (September (S1)) (2017) S225–S230, https://doi.org/10.1017/S0885715617000276.

[49] C. Önneby, C.G. Pantano, Silicon oxycarbide formation on SiC surfaces and at the SiC/SiO2 interface, J. Vac. Sci. Technol. Vac. Surf. Films 15 (May (3)) (1997) 1597–1602, https://doi.org/10.1116/1.580951.

[50] M.S. Donley, D.R. Baer, T.G. Stoebe, Nitrogen 1s charge referencing for Si3N4 and related compounds, Surf. Interface Anal. 11 (April (6–7)) (1988) 335–340, https://doi.org/10.1002/sia.740110611.

[51] Y. Iwase, Y. Horie, Y. Daiko, S. Honda, Y. Iwamoto, Synthesis of a novel polyethoxysilsesquiazane and thermal conversion into ternary silicon oxynitride ceramics with enhanced thermal stability, Materials 10 (December (12)) (2017), https://doi.org/10.3390/ma10121391, p. 1391.

[52] R. Weeren, E.A. Leone, S. Curran, L.C. Klein, S.C. Danforth, Synthesis and characterization of amorphous Si2N2O, J. Am. Ceram. Soc. 77 (October (10)) (1994) 2699–2702, https://doi.org/10.1111/j.1151-2916.1994.tb04664.x.

[53] D. Bouvet, et al., Influence of nitrogen profile on electrical characteristics of furnace- or rapid thermally nitrided silicon dioxide films, J. Appl. Phys. 79 (May (9)) (1996) 7114–7122, https://doi.org/10.1063/1.361481.

[54] J. Rouquerol et al., Recommendations for the Characterization of Porous Solids. De Gruyter, doi: 10.1515/iupac.66.0925.

[55] F. Rouquerol, J. Rouquerol, K.S.W. Sing, P.L. Llewellyn, G. Maurin (Eds.), Adsorption by Powders and Porous Solids: Principles, Methodology and Applications, 2nd ed., Elsevier/Academic Press, Amsterdam, 2014.

[56] Y. Shiozaki, E. Nakamura, T. Mitsui (Eds.), Inorganic Substances Other than Oxides. Part 1: SbSI Family … TAAP, vol. 36B1, Springer-Verlag, Berlin/Heidelberg, 2004.

[57] T. Bauer, D. Laing, R. Tamme, Characterization of sodium nitrate as phase change material, Int. J. Thermophys. 33 (January (1)) (2012) 91–104, https://doi.org/10.1007/s10765-011-1113-9.

[58] B. DAguanno, M. Karthik, A.N. Grace, A. Floris, Thermostatic properties of nitrate molten salts and their solar and eutectic mixtures, Sci. Rep. 8 (December (1)) (2018), https://doi.org/10.1038/s41598-018-28641-1, p. 10485.

[59] P. Ballirano, Laboratory parallel-beam transmission X-ray powder diffraction investigation of the thermal behavior of nitratine NaNO3: spontaneous strain and structure evolution, Phys. Chem. Miner. 38 (July (7)) (2011) 531–541, https://doi.org/10.1007/s00269-011-0425-4.

[60] T. Jriri, J. Rogez, C. Bergman, J.C. Mathieu, Thermodynamic study of the condensed phases of NaNO3, KNO3 and CsNO3 and their transitions, Thermochim. Acta 266 (November) (1995) 147–161, https://doi.org/10.1016/0040-6031(95)02337-2.

[61] G. Xu, et al., Sodium nitrate – diatomite composite materials for thermal energy storage, Sol. Energy 146 (April) (2017) 494–502, https://doi.org/10.1016/j.solener.2017.03.003.

[62] R. Schmidt, E.W. Hansen, M. Stoecker, D. Akporiaye, O.H. Ellestad, Pore size determination of MCM-51 mesoporous materials by means of 1H NMR spectroscopy, N2 adsorption, and HREM. A preliminary study, J. Am. Chem. Soc. 117 (April (14)) (1995) 4049–4056, https://doi.org/10.1021/ja00119a021.

[63] L. Feng, W. Zhao, J. Zheng, S. Frisco, P. Song, X. Li, The shape-stabilized phase change materials composed of polyethylene glycol and various mesoporous matrices (AC, SBA-15 and MCM-41), Sol. Energy Mater. Sol. Cells 95 (December (12)) (2011) 3550–3556, https://doi.org/10.1016/j.solmat.2011.08.020.

[64] K. Ishikiriyama, M. Todoki, K. Motomura, Pore size distribution (PSD) measurements of silica gels by means of differential scanning calorimetry, J. Colloid Interface Sci. 171 (April (1)) (1995) 92–102, https://doi.org/10.1006/jcis.1995.1154.

[65] R. Delhez, Th.H. de Keijser, E.J. Mittemeijer, Determination of crystallite size and lattice distortions through X-ray diffraction line profile analysis: Vorschriften, Methoden und Bemerkungen, Fresenius Z. Für Anal. Chem. 312 (January (1)) (1982) 1–16, https://doi.org/10.1007/BF00482725.

[66] A. Viard, D. Fonblanc, M. Schmidt, A. Lale, C. Salameh, A. Soleilhavoup, et al., Molecular chemistry and engineering of boron-modified polyorganosilazanes as new processable and functional SiBCN precursors, Chem. – Eur. J. 23 (2017) 9076–9090, https://doi.org/10.1002/chem.201700623.

[67] B.D. Bond, P.W.M. Jacobs, The thermal decomposition of sodium nitrate, J. Chem. Soc. Inorg. Phys. Theor. (1966), https://doi.org/10.1039/j19660001265, p. 1265.

[68] G. R. Pickrell, T. Sun, and J. J. Brown, High temperature alkali corrosion of Sic and S&N4, p. 24.

[69] R.G. Munro, S.J. Dapkunas, Corrosion characteristics of silicon carbide and silicon nitride, J. Res. Inst. Stand. Technol. 98 (September (5)) (1993), https://doi.org/10.6028/jres.098.040, p. 607.

[70] A.M. Goitandia, G. Beobide, E. Aranzabe, A. Aranzabe, Development of content-stable phase change composites by infiltration into inorganic porous supports, Sol. Energy Mater. Sol. Cells 134 (March) (2015) 318–328, https://doi.org/10.1016/j.solmat.2014.12.010.

[71] H. Gao, et al., Ambient pressure dried flexible silica aerogel for construction of monolithic shape-stabilized phase change materials, Sol. Energy Mater. Sol. Cells 201 (October) (2019), https://doi.org/10.1016/j.solmat.2019.110122, p. 110122.

[72] H. Gao, et al., Nanoconfinement effects on thermal properties of nanoporous shape-stabilized composite PCMs: a review, Nano Energy 53 (November) (2018) 769–797, https://doi.org/10.1016/j.nanoen.2018.09.007.

[73] Y. Zhang, S. Zheng, S. Zhu, J. Ma, Z. Sun, M. Farid, Evaluation of paraffin infiltrated in various porous silica matrices as shape-stabilized phase change materials for thermal energy storage, Energy Convers. Manage. 171 (September) (2018) 361–370, https://doi.org/10.1016/j.enconman.2018.06.002.

[74] A.L. Patterson, The Scherrer formula for X-ray particle size determination, Phys. Rev. 56 (November (10)) (1939) 978–982, https://doi.org/10.1103/PhysRev.56.978.

[75] G. Fredi, S. Dirè, E. Callone, R. Ceccato, F. Mondadori, A. Pegoretti, Docosane-organosilica microcapsules for structural composites with thermal energy storage/release capability, Materials 12 (April (8)) (2019), https://doi.org/10.3390/ma12081286, p. 1286.

[76] M. Lamvik, J.M. Zhou, Experimental study of thermal conductivity of solid and liquid phases at the phase transition, Int. J. Thermophys. 16 (March (2)) (1995) 567–576, https://doi.org/10.1007/BF01441922.

[77] Y. Deng, J. Li, H. Nian, Expanded vermiculite: a promising natural encapsulation material of LiNO 3, NaNO 3, and KNO 3 phase change materials for medium-temperature thermal energy storage, Adv. Eng. Mater. 20 (August (8)) (2018), https://doi.org/10.1002/adem.201800135, p. 1800135.

[78] G. Xu, et al., Sodium nitrate – diatomite composite materials for thermal energy storage, Sol. Energy 146 (April) (2017) 494–502, https://doi.org/10.1016/j.solener.2017.03.003.

[79] S. Chen, X. Cheng, H. Zheng, H. Zhong, Y. Li, and X. Wang, Study on the microstructures and thermal properties of SiO2@NaNO3 microcapsule thermal storage materials, p. 15.

[80] X. Li, H. Chen, L. Liu, Z. Lu, J.G. Sanjayan, W.H. Duan, Development of granular expanded perlite/paraffin phase change material composites and prevention of leakage, Sol. Energy 137 (November) (2016) 179–188, https://doi.org/10.1016/j.solener.2016.08.012.

[81] A. Karaipekli, A. Biçer, A. Sarı, V.V. Tyagi, Thermal characteristics of expanded perlite/paraffin composite phase change material with enhanced thermal conductivity using carbon nanotubes, Energy Convers. Manage. 134 (Febuary) (2017) 373–381, https://doi.org/10.1016/j.enconman.2016.12.053.

[82] X. Li, J.G. Sanjayan, J.L. Wilson, Fabrication and stability of form-stable diatomite/paraffin phase change material composites, Energy Build. 76 (June) (2014) 284–294, https://doi.org/10.1016/j.enbuild.2014.02.082.

[83] C. Li, L. Fu, J. Ouyang, A. Tang, H. Yang, Kaolinite stabilized paraffin composite phase change materials for thermal energy storage, Appl. Clay Sci. 115 (October) (2015) 212–220, https://doi.org/10.1016/j.clay.2015.07.033.